

# GPU-based Low Dose CT Reconstruction via Edge-preserving Total Variation Regularization<sup>†</sup>

Zhen Tian<sup>1,3</sup>, Xun Jia<sup>2,3</sup>, Kehong Yuan<sup>1</sup>, Tinsu Pan<sup>4</sup>, Steve B. Jiang<sup>2,3</sup>

5                   <sup>1</sup>Department of Biomedical Engineering, Graduate School at Shenzhen, Tsinghua  
University, Shenzhen, Guangdong 518055, China

<sup>2</sup>Department of Radiation Oncology, University of California San Diego, La Jolla,  
CA 92093, USA

10                   <sup>3</sup>Center for Advanced Radiotherapy Technologies, University of California San  
Diego, La Jolla, CA 92093, USA

<sup>4</sup>Department of Imaging Physics, University of Texas M. D. Anderson Cancer  
Center, Houston, Texas 77030, USA

Email: [sbjiang@ucsd.edu](mailto:sbjiang@ucsd.edu)

15

20                   High radiation dose in CT scans increases a lifetime risk of cancer and has become  
a major clinical concern. Recently, iterative reconstruction algorithms with Total  
Variation (TV) regularization have been developed to reconstruct CT images from  
highly undersampled data acquired at low mAs levels in order to reduce the  
imaging dose. Nonetheless, TV regularization may lead to over-smoothed images  
and lost edge information. To solve this problem, in this work we develop an  
iterative CT reconstruction algorithm with edge-preserving TV regularization to  
25                   reconstruct CT images from highly undersampled data obtained at low mAs levels.  
The CT image is reconstructed by minimizing an energy consisting of an  
edge-preserving TV norm and a data fidelity term posed by the x-ray projections.  
The edge-preserving TV term is proposed to preferentially perform smoothing only  
on non-edge part of the image in order to avoid over-smoothing, which is realized  
30                   by introducing a penalty weight to the original total variation norm. Our iterative  
algorithm is implemented on GPU to improve its speed. We test our reconstruction

---

<sup>†</sup> Zhen Tian and Xun Jia have contributed equally to this work and should be considered co-first authors.

algorithm on a digital NCAT phantom, a physical chest phantom, and a Catphan phantom. Reconstruction results from a conventional FBP algorithm and a TV regularization method without edge preserving penalty are also presented for comparison purpose. The experimental results illustrate that both TV-based algorithm and our edge-preserving TV algorithm outperform the conventional FBP algorithm in suppressing the streaking artifacts and image noise under the low dose context. Our edge-preserving algorithm is superior to the TV-based algorithm in that it can preserve more information of fine structures and therefore maintain acceptable spatial resolution.

5

10

## 1. Introduction

X-ray computed tomography (CT) has been extensively used in clinics to provide patient volumetric images for a number of purposes nowadays. However, by its nature, CT scans expose  
5 a high x-ray radiation dose to the patient which may result in a non-negligible lifetime risk of cancer (Hall and Brenner, 2008; de Gonzalez *et al.*, 2009; Smith-Bindman *et al.*, 2009). This fact has become a major concern for the clinical applications of CT scans, particularly for pediatric patients, who are more sensitive to radiation and have a longer life expectancy than adults (Brenner *et al.*, 2001; Brody *et al.*, 2007; Chodick *et al.*, 2007). Therefore, it is highly desirable  
10 to reduce CT imaging dose while maintaining clinically acceptable image quality.

A simple way to reduce the x-ray dose is to lower mAs levels in CT data acquisition protocols. Nonetheless, this approach will result in an insufficient number of x-ray photons detected at imager and hence elevate the quantum noise level on the sinogram. As a consequence, the quality of the CT images reconstructed from a conventional filtered backprojection (FBP)  
15 algorithm (Deans, 1983) will be degraded by the noise-contaminated sinogram data. Another way to reduce imaging dose is to decrease the number of x-ray projections acquired by, *e.g.*, operating the x-ray generator in the pulsed model at a low frequency. Yet, this will cause serious streaking artifacts in the reconstructed CT images, as the FBP algorithms require that the number of projections should satisfy the Shannon sampling theorem (Jerri, 1977).

20 Recently, compressed sensing algorithms (Donoho, 2006) have been applied to the CT reconstruction problem. In particular, Total Variation (TV) methods (Rudin *et al.*, 1992) have presented their tremendous power in CT reconstruction with only a few x-ray projections (Sidky *et al.*, 2006; Song *et al.*, 2007; Chen *et al.*, 2008; Sidky and Pan, 2008). In such approaches, an energy function of a TV form is minimized subject to a data fidelity condition posed by the x-ray  
25 projections. Since this energy term corresponds to image gradient, minimizing it will effectively remove those high spatial gradient parts such as noise and streaking artifacts in the reconstructed CT images. One disadvantage of this TV approach is its tendency to uniformly penalize the image gradient irrespective of the underlying image structures. As a result, the reconstructed images are usually over-smoothed and edges of fine structures are smeared. As the edge  
30 information in medical imaging is of crucial importance in a number of diagnostic applications, the image quality in the TV-based CT reconstruction approach is sometimes clinically unacceptable. To resolve this issue, an edge guided compressive sensing reconstruction algorithm has recently been proposed in solving an MRI image reconstruction problem (Guo and Yin, 2010). In such an approach, edges are detected during the reconstruction process and are  
35 purposely excluded from being smoothed by the TV norm. Though this method can be easily generalized to the CT reconstruction problems, when it comes to the undersampling case where insufficient x-ray projections are used in the reconstruction, a high quality edge detection algorithm is required to avoid incorrect detection of those fake edges caused by noise and streaking artifacts. The sophisticated edge detection algorithms usually pose a high computation  
40 burden in the reconstructions. Moreover, they may require fine tuning of some case dependent parameters, making it hard to control their efficacy.

Another disadvantage of the TV-based reconstruction methods are the associated time consuming computation process due to their iterative nature. Generally speaking, the prolonged computational time makes the iterative CT reconstruction approaches prohibitive in many routine

clinical applications. Recently, high-performance graphics processing units (GPUs) have been reported to speed up heavy duty computational tasks in medical physics, such as CBCT reconstruction (Xu and Mueller, 2005, 2007; Li *et al.*, 2007; Yan *et al.*, 2008; Jia *et al.*, 2010b), deformable image registration (Sharp *et al.*, 2007; Samant *et al.*, 2008; Gu *et al.*, 2010), dose calculation (Gu *et al.*, 2009; Hissoiny *et al.*, 2009; Jia *et al.*, 2010a) and treatment plan optimization (Men *et al.*, 2009; Men *et al.*, 2010). In principle, high computation efficiency can be expected utilizing GPU in our CT reconstruction problem.

In this work, we generalize the TV-based CT reconstruction algorithm to an edge-preserving TV (EPTV) regularization form to reconstruct CT images from highly undersampled projections acquired at low mAs level. In particular, an EPTV norm is designed by introducing a penalty weight to the original TV norm, which enables the algorithm to locate the sharp discontinuities of image intensity and adjust the weight adaptively to adopt the progressively recovered edge information during the reconstruction process. This regularization term automatically ensures that less smoothing is performed on edges, preventing them from being over-smoothed, as will be seen in below. Our reconstruction algorithm is implemented on GPU to speed up the computation process.

## 2. Methods

### 2.1 Reconstruction Model

CT projection can be mathematically formulated as a linear equation,

$$Pf = y, \quad (1)$$

where  $f$  is a vector whose entries correspond to the x-ray linear attenuation coefficients at different voxels of the patient image.  $P$  is a projection matrix in fan-beam geometry and can be explicitly computed. The vector  $y$  represents the log-transformed projection data measured on image detectors at various projection angles. A CT reconstruction problem is formulated as to retrieve the unknown vector  $f$  based on the projection matrix  $P$  and the observation vector  $y$ . When it comes to an undersampled problem where inadequate projection data is used to reconstruct the CT image, the problem become underdetermined and there exist infinitely many solutions to the Eq. (1).

As opposed to solve the linear equation directly, the CT image can be reconstructed by minimizing an energy function with a TV regularization term:

$$f = \operatorname{argmin}_f E(f) = \operatorname{argmin}_f \frac{\mu}{2} \|Pf - y\|_2^2 + J(f), \quad s. t. f_i \geq 0 \text{ for } \forall i, \quad (2)$$

where  $\|\cdot\|_n$  denotes the  $l_n$  vector norm in the imager vector space. In Eq. (2), the first term is known as a data fidelity term, which ensures the consistency between the reconstructed image  $f$  and the measurement  $y$ . The second one is a regularization term, which is chosen to be a TV semi-norm. The introduction of the TV term in this optimization process differentiates those infinite many solutions to the Eq. (1) and picks out the one with desired image properties as the reconstructed image. Specifically, the TV term is defined as

$$J(f) = \|f\|_{TV} = \int \|\nabla f(x)\|_1 dx , \quad (3)$$

where  $\nabla f(x)$  represents the gradient of an image  $f$  at a pixel  $x$ . The TV term has been shown to be robust to remove noise and artifacts in the reconstructed image  $f$  (Sidky and Pan, 2008; Jia *et al.*, 2010b). A scalar  $\mu$  is introduced to adjust the relative weights between the data fidelity term and the regularization term.

5 In this minimization problem, the TV norm is induced for the purpose of image smoothing and noise reduction, as it gives a large penalty to those images with large gradient values. However, this TV term uniformly penalizes the gradient everywhere on the entire image regardless of the underlying image structure, leading to over-smoothing of the reconstructed image and losing of edge information. To overcome this limitation, we propose an EPTV  
10 regularization term by introducing a penalty weight vector  $\omega$  in defining the TV term, namely

$$J(f) = \|f\|_{EPTV} = \int \omega(x) \|\nabla f(x)\|_1 dx . \quad (4)$$

Specifically, we assign a small weight  $\omega(x)$  if the gradient value of at the pixel  $x$  is large and vice versa. Since those pixels with large gradients are likely to be edges in the CT image, our approach enables that less amount of smoothing is applied at those pixels. On the other hand, more smoothing is performed on the pixels with small gradients which are likely due to image  
15 noise. By this means, the algorithm preferentially performs smoothing on those non-edge pixels to reduce image noise while keeping those sharp edges unaffected. As such, we define  $\omega(x)$  as

$$\omega(x) = \exp[-(\|f(x)\|_{TV}/\sigma)^2] , \quad (5)$$

where the parameter  $\sigma$  controls the amount of smoothing that we would like to apply to those non-edge pixels relative to those edge pixels. Apparently, the choice of  $\sigma$  is of central importance for the algorithm. A large  $\sigma$  is not able to differentiate image gradients at different  
20 pixels. In such a circumstance, the algorithm becomes essentially the TV method, compromising the effect of our EPTV algorithm. In contrast, small  $\sigma$  tends to give small weights to almost every pixel, making the EPTV norm inefficient in removing noise or streaking artifacts. Since the gradient values changes during the iterative reconstruction process, we propose to adaptively set the value of  $\sigma$  according to the histogram of the gradient magnitude. In particular, for the  
25 test cases in this paper,  $\sigma$  is chosen such that 90%~95% pixels have the values of TV norm smaller than  $\sigma$ , as we found this choice is a good balance between reconstruction efficiency and image quality.

## 2.2 Optimization Approach

30

The main challenge to solve the minimization problem is due to the projection matrix  $P$  which is sparse but still huge. If a simple gradient descent approach is used,  $P$  would be both involved in computing a search direction and searching for a step length. This repeated computing of this matrix lead to prolonged computation time. In this paper, we utilize a forward-backward splitting  
35 (Combettes and Wajs, 2005; Hale *et al.*, 2008) algorithm to overcome this problem by splitting the minimization into two parts, while the computation of the projection matrix  $P$  is needed only in one of them. The algorithm is described as follows:

---

Algorithm 1:

---

Initialize  $f^{(0)} = 0$ . For  $k = 1, 2, \dots$ , do the following steps until convergence.

1. Solve (P1):  $v^{(k)} = \operatorname{argmin}_f \|Pf - y\|_2^2$  with CGLS solver and an initial value  $f^{(k)}$ .
  2. Update the penalty weight:  $\omega(x) = \exp(-\|v^{(k)}(x)\|_{TV}^2/\sigma^2)$ .
  3. Solve (P2):  $f^{(k+1)} = \operatorname{argmin}_f \frac{\mu}{2} \|f - v^{(k)}\|_2^2 + \|f\|_{EPTV}$  with GD method.
  4. Ensuring image positivity:  $f^{(k+1)} = 0$  if  $f^{(k+1)} < 0$ .
- 

Step 4 implements a simple truncation of pixel values to ensure the positivity of the reconstructed images, as physically those pixel values are x-ray attenuation coefficients and has to be positive. As for the optimization problem (P1) in step 1, we use conjugate gradient least square (CGLS) method (Hestenes and Stiefel, 1952). These steps are performed until the algorithm converges to a relatively stable solution or exceeds the certain iteration steps.

It is worth mentioning that in step 3 we solve the minimization problem (P2) with a simple gradient descent (GD) method in an iterative manner. At each iteration, the gradient direction  $g$  is first numerically calculated. An inexact line search is then performed along the negative gradient direction and a step size is determined according to Amijo's rule (Bazaraa *et al.*, 2006). The solution is then updated accordingly. The gradient direction  $g$  is calculated as:

$$g = \mu(f - v^{(k)}) + \frac{\partial}{\partial f} \|f\|_{EPTV}, \quad (6)$$

$$\frac{\partial}{\partial f} \|f\|_{EPTV} = -\nabla \left( \frac{\omega(x)\nabla f}{\|f(x)\|_{TV}} \right).$$

Numerically, we approximate the gradient term of EPTV by a symmetric finite difference scheme

$$\begin{aligned} \frac{\partial}{\partial f_{i,j}} \|f\|_{EPTV} \approx & - \left[ \frac{\omega_{i+1/2,j}(f_{i+1,j} - f_{i,j})}{\|f_{i+1/2,j}\|_{TV}} - \frac{\omega_{i-1/2,j}(f_{i,j} - f_{i-1,j})}{\|f_{i-1/2,j}\|_{TV}} \right] \\ & - \left[ \frac{\omega_{i,j+1/2}(f_{i,j+1} - f_{i,j})}{\|f_{i,j+1/2}\|_{TV}} - \frac{\omega_{i,j-1/2}(f_{i,j} - f_{i,j-1})}{\|f_{i,j-1/2}\|_{TV}} \right] \end{aligned} \quad (7)$$

where,

$$\begin{aligned} \|f_{i+1/2,j}\|_{TV} &= \left[ (f_{i+1,j} - f_{i,j})^2 + \frac{1}{2}(f_{i+1/2,j+1} - f_{i+1/2,j})^2 \right. \\ &\quad \left. + \frac{1}{2}(f_{i+1/2,j} - f_{i+1/2,j-1})^2 \right]^{1/2}, \\ f_{i+1/2,j} &= \frac{1}{2}(f_{i+1,j} + f_{i,j}), \\ \omega_{i+1/2,j} &= \exp\left(-\frac{\|f_{i+1/2,j}\|_{TV}^2}{\sigma^2}\right). \end{aligned} \quad (8)$$

Such an approximation scheme, though cumbersome, ensures the stability of the algorithm.

### 15 2.3 Details in CUDA implementation

Our GPU-based reconstruction code was developed under the Compute Unified Device Architecture (CUDA) programming environment and GPU hardware platform. This platform enables a number of tasks implemented in parallel on different CUDA threads simultaneously, which speeds up the performance of our reconstruction algorithm. In our algorithm, the sub-optimization problem ( $P1$ ) of step1 in Algorithm 1 involves lots of sparse matrix-vector multiplication. We adopted the fast GPU sparse matrix-vector multiplication (Bell and Garland, 2008) to perform this task. Other vector-vector and scalar-vector operations encountered in this step were accomplished with CUBLAS (NVIDIA, 2008), yielding high computation efficiency. Besides, the penalty weight  $\omega$  and the gradient vector  $g$  can also be calculated in parallel with each thread computing one of its entries at the same time. The flow chart of our reconstruction algorithm is shown in Fig. 1.

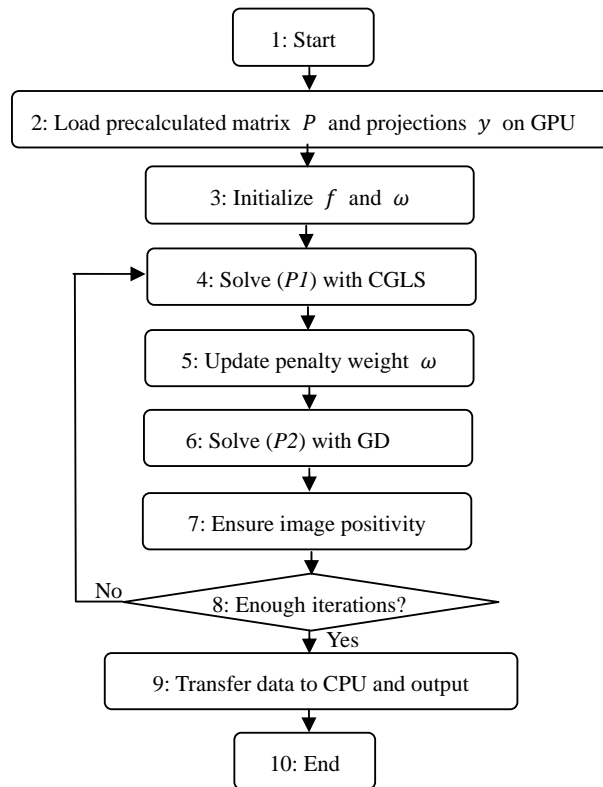


**Figure 1.** The flow chart of our GPU-based EPTV reconstruction. Blocks 4~7 correspond to the steps 1~4 in Algorithm 1.

15

### 3. Experimental Results

We tested our reconstruction algorithm on three cases: a digital NURBS-based cardiac-torso (NCAT) phantom in thorax region (Segars, 2002), a physical chest phantom, and a Catphan phantom. In digital phantom experiments, we simulated x-ray projections using Siddon's ray tracing algorithm (Siddon, 1985) in fan-beam geometry with an arc detector of 888 units and a spacing of 1.0239mm. The source to detector distance is 949.075mm and the source to rotation center distance is 541.0mm. All of these parameters mimic a realistic configuration of a GE

20

Lightspeed QX/I CT scanner. In all cases, we simulated/acquired x-ray projection data along 984 directions equally spaced in a full rotation and a subset of them were used for reconstruction. The size of reconstructed images is  $512 \times 512$ .

### 5 3.1 Digital phantom experiment

We first tested our EPTV algorithm on an NCAT phantom in thorax region using undersampled x-ray projections. The reconstructed images using 40 projections are shown in Fig. 2. We can see that the conventional FBP algorithm is not able to reconstruct the CT images with such few projections and obvious streaking artifacts are observed, which makes the image unacceptable. In contrast, even with such few projections, both the TV method and the EPTV method can still capture most of the structures, leading to visually much better reconstruction results. As for the comparison between the TV method and the EPTV method, the spinal bone structures of low contrast indicated by the arrow in Fig. 2 (c) and (d) are hardly resolved by the TV method, while much clearer structures with sharper edges are observed in the image reconstructed by the EPTV method. To better compare the TV method and the EPTV method in detail, we also show the horizontal and vertical intensity profiles going through the center of the reconstructed images. Clearly, large fluctuations at non-edge points are observed in the profiles obtained from the TV method. Besides, the jumps indicated by arrows are broadened and weakened, indicating blurring effects and losing of contrast. On the other hand, the profiles of EPTV are very close to that of the ground truth with sharp jumps at edge points and small fluctuation at non-edge points. All of these clearly demonstrate the advantages of the EPTV algorithm in preserving edge over the TV algorithm.

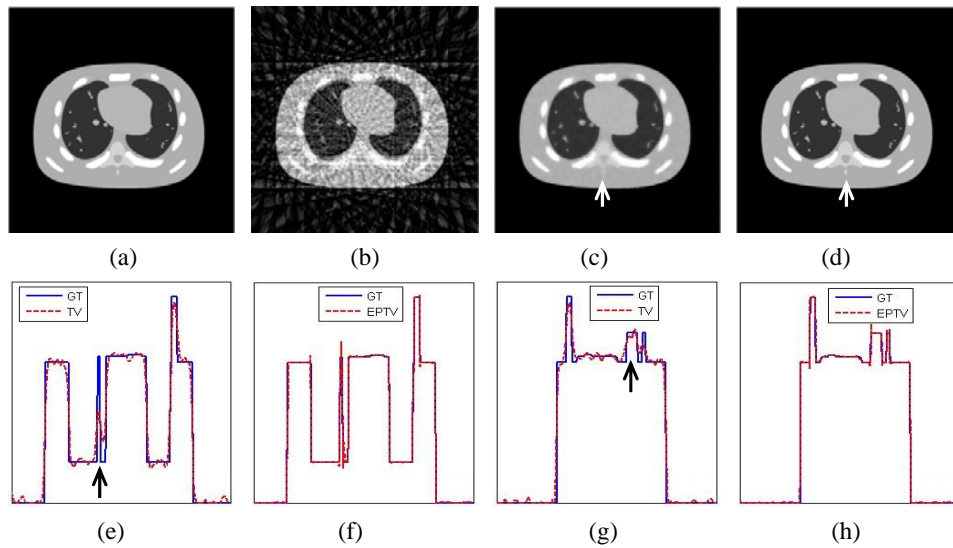


**Figure 2.** The reconstruction results of NCAT phantom using 40 projections. (a) is the ground truth image. (b) ~ (d) show the images reconstructed by FBP, TV, EPTV, respectively. (e)(f) depict the horizontal intensity profiles through the center of reconstructed images of TV and EPTV, while (g)(h) are the corresponding vertical intensity profiles. The profiles of ground truth (GT) are also plotted in solid lines for comparison. The arrows indicate the area where EPTV is clearly superior to TV.

To quantify the reconstruction accuracy of the algorithm, we use relative error as a metric to

measure the similarity between the ground truth image and reconstructed image. Besides, since edge information is an important feature of images and human vision is highly sensitive to it, edge cross-correlation coefficient (ECC) (Xu and Mueller, 2009) is also used as another metric to evaluate the reconstruction accuracy. These metrics are calculated as follows:

$$e = \frac{\|f - f^*\|_2^2}{\|f^*\|_2^2}$$

$$c = \frac{\sum_i (b_i - \bar{b})(b_i^* - \bar{b}^*)}{\sqrt{\sum_i (b_i - \bar{b})^2 \sum_j (b_j^* - \bar{b}^*)^2}} \quad (9)$$

5 where  $f^*$  is the ground truth image and  $b$  is a binary image with 1 indexing image edges on the reconstructed image and 0 otherwise. The edges are detected using a standard Sobel edge detector (Kanopoulos *et al.*, 1988).  $b^*$  is defined in a similar manner for the ground truth image. The over-bar indicates an average of the corresponding quantities over all pixels.

10 The relative error  $e$  and the edge correlation coefficient  $c$  of the reconstructed images of the digital phantom are shown as functions of number of projections and number of iterations, respectively, in Fig. 3. As expected, the more projections used, the better reconstruction quality will be obtained with smaller relative error and higher edge correlation coefficient. Fig. 3(a) and (b) clearly demonstrate that with the same number of projections, the EPTV method is superior to the TV method with a smaller error and higher edge cross-correlation. We can also see that, in  
15 this particular case, 40 projections are sufficient for EPTV reconstruction. The evolution curves of the relative error and the edge correlation during iterations in Fig. 3(c) and (d) show that the EPTV algorithm converges much faster than the TV method. With these curves, we can conclude that the EPTV method outperforms the TV method, in that it leads to smaller relative error, higher correlation, and faster convergence for a given number of projections.

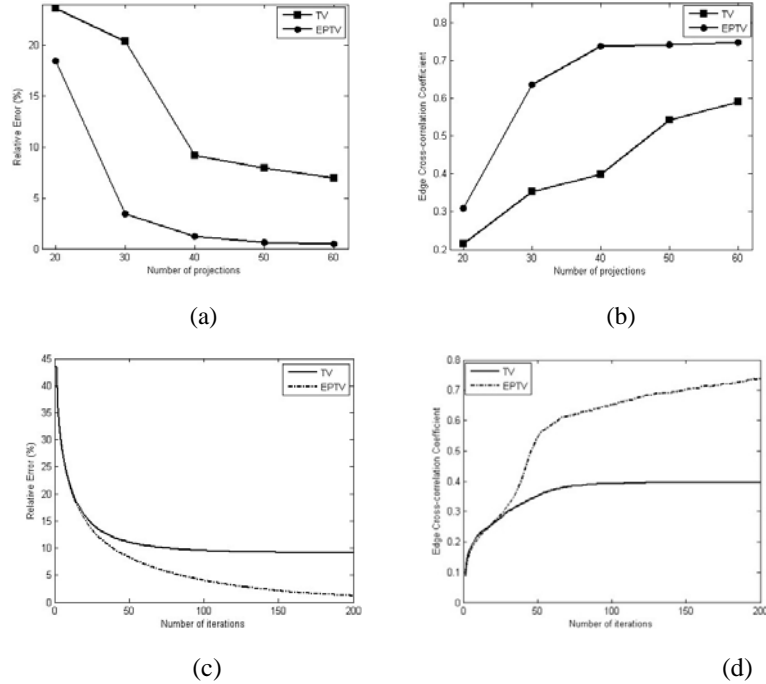


**Figure 3.** (a)(b) show the relative error and the edge cross-correlation coefficient as functions of the

number of x-ray projections at 200 iteration steps; (c)(d) show the evolution curve of the relative error and the edge cross correlation during the first 200 iterations using 40 projections.

### 3.2 Physical phantom experiments

- 5 In this paper, we scanned both a physical chest phantom and a physical Catphan phantom under high dose and low dose protocols. The experiment on the chest phantom was designed to evaluate the tolerance of the EPTV algorithm to image noise due to low imaging dose, while the experiment on the Catphan phantom aimed to evaluate the performance of our algorithm in terms of spatial resolution.
- 10 In the experiment on the chest phantom, for the high dose protocol, 984 projections with 0.4mAs/projection were acquired and then used to reconstruct the image with the FBP algorithm. In the low dose protocol, the chest phantom was scanned at 0.02mAs/projection and only 200 equally spaced projections are used for reconstruction. The dose in the low dose protocol is about 1% of that in the high dose protocol. The reconstruction results are shown in Fig. 4. We can see
- 15 that using FBP in such a low dose situation, the image quality deteriorates greatly with obvious streaking artifacts and image noise, which makes the reconstructed images unsatisfactory for clinic. In contrast, images reconstructed by TV and EPTV under the same low dose context show better image quality with less noise and streaking artifacts. While comparing TV and EPTV methods, the latter is found to be superior on edge preserving and lead to sharper CT images.
- 20 Take the area indicated by the arrows as an example, the cavity inside bones are almost invisible due to the blurring effect in the image reconstructed by TV, while the EPTV method can still preserve the hollow structures.

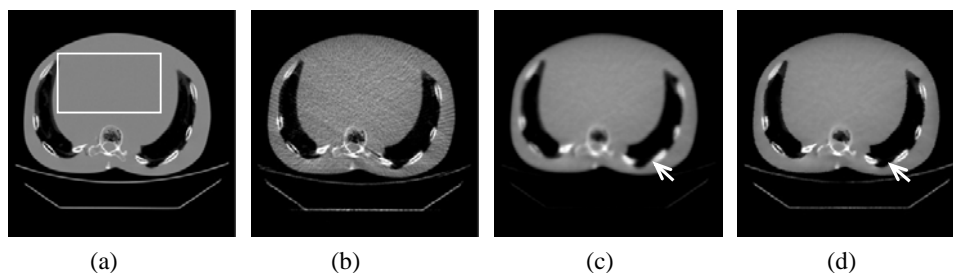


**Figure 4.** Reconstruction results of a physical chest phantom. (a) shows the image reconstructed by FBP at 400mAs (984 projections  $\times$  0.407mAs/projection). (b), (c), and (d) show the images reconstructed by FBP, TV, EPTV, respectively, at 4mAs (200 projections  $\times$  0.0203mAs/projection). The rectangle shows ROI used for SNR calculation. Arrows indicate the area where EPTV is clearly superior to TV.

To quantify the image quality of reconstructed images in terms of image noise, the signal to noise ratio (SNR) of a region of interest (ROI) is shown in Table 1. The calculation is as follows:

$$SNR = 10 \times \log_{10} \left[ \frac{E^2(P)}{E([P-E(P)]^2)} \right], \quad (7)$$

- 25 where  $p$  is the set of pixels inside the ROI and  $E(\cdot)$  stands for a spatial average over the ROI. It can be observed from Table 1 that when the imaging dose is decreased by 100 times, the SNR of images reconstructed by FBP is lowered from 40.6 to 19.0, indicating the sensitivity of the FBP method to image noise and its inability to handle the low dose situation. In contrast, the

SNRs of images reconstructed by TV and EPTV methods are only decreased by a little compared to images reconstructed by FBP with high dose. With these results, we can conclude that our EPTV method not only outperforms the TV method on edge preserving, but also inherits the advantage of the TV method on handling the low dose situation and effectively suppressing image noise.

	FBP	FBP	TV	EPTV
mAs	400	4	4	4
SNR	40.6	19.0	35.4	35.5

**Table 1.** SNR of the ROI in the reconstructed images of the chest phantom.

The experimental results of the Catphan phantom are shown in Fig. 5. The low imaging dose in this case is 8mAs, about 2% of that in the high dose scan, by decreasing the number of projections from 984 to 400 and reducing the mAs/projection from 0.4 to 0.02 mAs/projection. The sixth line pair at which the arrows point clearly demonstrate the different performances of the three reconstruction algorithms in terms of resolution. For the FBP reconstruction at low dose, the sixth line pair can still be clearly resolved as in Fig. 5(f). Compared with the reconstructed image of high dose, the low dose image reconstructed by FBP deteriorates mainly due to image noise, but still maintains good spatial resolution (6.5 lp/cm). On the other hand, although the TV method performs well in suppressing the image noise, the spatial resolution is degraded to 4 lp/cm. The sixth pair of lines is blurred and cannot be visually resolved, see Fig. 5(g). Finally, for the image reconstructed by the EPTV method, it contains less noise and maintains high spatial resolution (6.5 lp/cm), where the lines in the sixth pair can be clearly identified from each other in Fig. 5(h). The results of this test confirm the conclusion that, not only does our EPTV method effectively reduce image noise in low dose CT reconstruction, but also performs better than TV in maintaining acceptable spatial resolution.

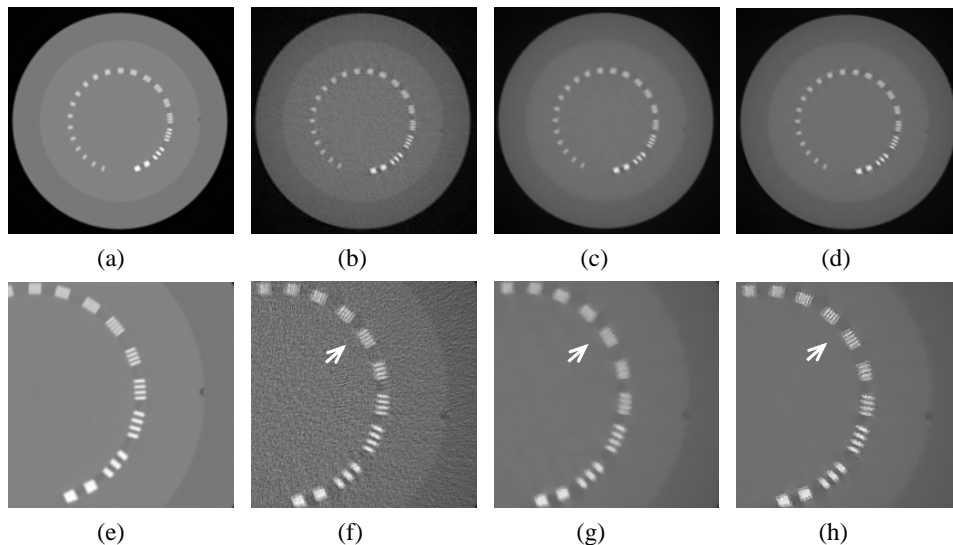


Figure 5. Reconstruction results of the Catphan phantom. (a) shows the image reconstructed by FBP at 400mAs (984 projections $\times$ 0.407mAs/projection). (b), (c), and (d) show the images reconstructed by FBP, TV, EPTV, respectively, at 8mAs (400 projections $\times$ 0.0203mAs/projection). (e)-(h) zoom in the corresponding images on the first row. Arrows indicate the area where EPTV is clearly superior to TV.

### 3.3 Computation efficiency

To speed up our iterative algorithm, we have implemented and tested it on an NVIDIA Tesla C1060 card. For comparison purpose, the algorithm in C language was also implemented on a 2.27 GHz Intel Xeon processor. The computation times of the EPTV algorithm on CPU and GPU for an axial CT slice are shown in Table. 2. The absolute computation time is case dependent as it varies with the number of projections used ( $NP$ ), the number of iterations ( $NI$ ), *etc.* However, when comparing  $T_{CPU}$  and  $T_{GPU}$  for a same case, it is found that the algorithm is sped up by factors of about 19.6~23.1. This considerable enhancement of efficiency implies a potential application of the EPTV algorithm in a realistic clinical environment to reduce the imaging dose. Although currently the reconstruction time still cannot compete with that of the conventional FBP, it is hoped that multi-GPU would be used in future to implement the reconstruction for multiple slices simultaneously, which would speed up the algorithm further. We will also optimize the algorithm to further improve its efficiency.

	NP	NI	$T_{CPU}$ (s)	$T_{GPU}$ (s)	$T_{CPU}/T_{GPU}$
NCAT	40	100	253.8	11.0	23.1
Chest	200	50	353.8	16.4	21.5
Catphan	400	20	374.8	19.1	19.6

**Table 2.** The computation time of the EPTV algorithm on CPU and GPU.

#### 4. Conclusions

Two possible ways to reduce the imaging dose of CT scans are to reduce the number of projections and lower the mAs per projection. However, the common FBP reconstruction algorithms result in streaking artifacts and obvious image noises in these circumstances, which can be clearly observed in the experimental results. The iterative algorithm with TV norm as a regularization term has presented its tremendous power in CT reconstruction with undersampled projections acquired at low mAs level. However, since the TV term performs image smoothing and noise reducing by uniformly penalizing the gradient everywhere on the entire image, it sometimes results in over-smoothed edge in the reconstructed images and losing fine structural information. In this work, we propose an edge-preserving TV norm to solve the problem by giving different smoothing weights to pixels according to their gradient values. In particular, the weighting factors are adaptively adjusted during the reconstruction process. By this adaptive penalization mechanism, our algorithm preferentially performs smoothing on those non-edge pixels to reduce image noise while keeping those sharp edges unaffected. Our EPTV approach has been validated on a digital NCAT phantom, a physical chest phantom and also a Catphan phantom. The experimental results have clearly demonstrated the advantage of our approach over the conventional filtered backprojection algorithm and the TV-based reconstruction algorithm under low dose context on effectively suppressing image noise and streaking artifact and also maintaining acceptable signal-to-noise ratio and spatial resolution, which indicates a promising prospect of our low dose CT reconstruction algorithm in clinical applications for a considerable reduction of radiation dose exposed to patients.

GPU is employed in our experiments to improve the speed of this iterative algorithm, which is always a big challenge for the clinical applications of this type of algorithms. It is found that

the GPU implementation is able to speed up the iterative reconstruction process by factors of 19.6~23.1 and make it possible to reconstruct an image in seconds instead of minutes. Though currently the reconstruction speed still cannot compete with the speed of the conventional FBP, it is hoped that the efficiency can be improved by using multi-GPU and reconstructing multiple  
5 CT slices simultaneously in the near future. We would also work on optimizing our algorithm to improve the speed further.

### **Acknowledgements**

10 This work is supported in part by the University of California Lab Fees Research Program. The authors would like to thank NVIDIA for providing GPU cards for this project.

## References

- Bazaraa M, Sherali H and Shetty C 2006 *Nonlinear programming: theory and algorithms*: John Wiley and Sons)
- 5 Bell N and Garland M 2008 Efficient sparse matrix-vector multiplication on CUDA *NVIDIA Corporation, NVIDIA Technical Report NVR-2008-004*
- Brenner D J, Elliston C D, Hall E J and Berdon W E 2001 Estimated risks of radiation-induced fatal cancer from pediatric CT *American Journal of Roentgenology* **176** 289-96
- Brody A, Frush D, Huda W and Brent R 2007 Radiation risk to children from computed tomography  
10 *Pediatrics* **120** 677-82
- Chen G, Tang J and Leng S 2008 Prior image constrained compressed sensing (PICCS): a method to accurately reconstruct dynamic CT images from highly undersampled projection data sets  
*Medical Physics* **35** 660-3
- Chodick G, Ronckers C, Shalev V and Ron E 2007 Excess lifetime cancer mortality risk attributable  
15 to radiation exposure from computed tomography examinations in children *Medical Association Journal* **9** 584-7
- Combettes P and Wajs V 2005 Signal recovery by proximal forward-backward splitting *Multiscale Modeling and Simulation* **4** 1168-200
- de Gonzalez A B, Mahesh M, Kim K P, Bhargavan M, Lewis R, Mettler F and Land C 2009 Projected  
20 Cancer Risks From Computed Tomographic Scans Performed in the United States in 2007  
*Archives of Internal Medicine* **169** 2071-7
- Deans S R 1983 *The Radon transform and some of its applications*: Wiley)
- Donoho D 2006 Compressed sensing *IEEE Transactions on Information Theory* **52** 1289-306
- Gu X, Choi D, Men C, Pan H, Majumdar A and Jiang S 2009 GPU-based ultra-fast dose calculation  
25 using a finite size pencil beam model *Physics in medicine and biology* **54** 6287-97
- Gu X J, Pan H, Liang Y, Castillo R, Yang D S, Choi D J, Castillo E, Majumdar A, Guerrero T and Jiang S B 2010 Implementation and evaluation of various demons deformable image registration algorithms on a GPU *Physics in Medicine and Biology* **55** 207-19
- Guo W and Yin W 2010 EdgeCS: Edge Guided Compressive Sensing Reconstruction. In: *Rice CAAM Report TR10-02*,  
30
- Hale E, Yin W and Zhang Y 2008 Fixed-Point Continuation for  $l_1$ -Minimization: Methodology and Convergence *SIAM Journal on Optimization* **19** 1107-30
- Hall E J and Brenner D J 2008 Cancer risks from diagnostic radiology *Br. J. Radiol.* **81** 362-78
- Hestenes M and Stiefel E 1952 Methods of conjugate gradients for solving linear systems *Journal of  
35 Research of the National Bureau of Standards* **49** 409-36
- Hissoiny S, Ozell B and Despres P 2009 Fast convolution-superposition dose calculation on graphics hardware *Medical Physics* **36** 1998-2005
- Jerri A 1977 The Shannon sampling theorem-Its various extensions and applications: A tutorial review  
*Proceedings of the IEEE* **65** 1565-96
- 40 Jia X, Gu X, Sempau J, Choi D, Majumdar A and Jiang S 2010a Development of a GPU-based Monte Carlo dose calculation code for coupled electron-photon transport *Phys. Med. Biol* **55** 3077-86
- Jia X, Lou Y, Li R, Song W and Jiang S 2010b GPU-based fast cone beam CT reconstruction from undersampled and noisy projection data via total variation *Medical Physics* **37** 1757-60

- Kanopoulos N, Vasanthavada N and Baker R 1988 Design of an image edge detection filter using the sobel operator *IEEE Journal of solid-state circuits* **23** 358-67
- Li M, Yang H, Koizumi K and Kudo H 2007 Fast cone-beam CT reconstruction using CUDA architecture *Medical Imaging Technology* **25** 243-50
- 5 Men C, Gu X, Choi D, Majumdar A, Zheng Z, Mueller K and Jiang S 2009 GPU-based ultrafast IMRT plan optimization *Physics in medicine and biology* **54** 6565-73
- Men C, Jia X and Jiang S 2010 GPU-based ultra-fast direct aperture optimization for online adaptive radiation therapy *Phys. Med. Biol* **55** 4309-19
- NVIDIA C 2008 CUBLAS Library. NVIDIA Corporation, Santa Clara, California)
- 10 Rudin L, Osher S and Fatemi E 1992 Nonlinear total variation based noise removal algorithms *Physica D* **60** 259-68
- Samant S, Xia J, Muyan-Ozcelik P and Owens J 2008 High performance computing for deformable image registration: Towards a new paradigm in adaptive radiotherapy *Medical Physics* **35** 3546-53
- 15 Segars W 2002 Development of a new dynamic NURBS-based cardiac-torso (NCAT) phantom. In: *University of North Carolina: Chapel-hill*,
- Sharp G, Kandasamy N, Singh H and Folkert M 2007 GPU-based streaming architectures for fast cone-beam CT image reconstruction and demons deformable registration *Physics in medicine and biology* **52** 5771-84
- 20 Siddon R 1985 Fast calculation of the exact radiological path of a three-dimensional CT array *Medical Physics* **12** 252-5
- Sidky E, Kao C and Pan X 2006 Accurate image reconstruction from few-views and limited-angle data in divergent-beam CT *Journal of X-Ray Science and Technology* **14** 119-39
- Sidky E and Pan X 2008 Image reconstruction in circular cone-beam computed tomography by constrained, total-variation minimization *Phys. Med. Biol* **53** 4777-807
- 25 Smith-Bindman R, Lipson J, Marcus R, Kim K P, Mahesh M, Gould R, Berrington de Gonzalez A and Miglioretti D L 2009 Radiation dose associated with common computed tomography examinations and the associated lifetime attributable risk of cancer *Arch Intern Med* **169** 2078-86
- 30 Song J, Liu Q, Johnson G and Badea C 2007 Sparseness prior based iterative image reconstruction for retrospectively gated cardiac micro-CT *Medical Physics* **34** 4476-83
- Xu F and Mueller K 2005 Accelerating popular tomographic reconstruction algorithms on commodity PC graphics hardware *IEEE transactions on nuclear science* **52** 654-63
- Xu F and Mueller K 2007 Real-time 3D computed tomographic reconstruction using commodity graphics hardware *Physics in medicine and biology* **52** 3405-19
- 35 Xu W and Mueller K 2009 Learning Effective Parameter Settings for Iterative CT Reconstruction Algorithms. In: *Fully 3D Reconstruction in Radiology and Nuclear Medicine Conference*,
- Yan G, Tian J, Zhu S, Dai Y and Qin C 2008 Fast cone-beam CT image reconstruction using GPU hardware *Journal of X-Ray Science and Technology* **16** 225-34

40